Hydrothermal synthesis of SrTiO₃ nanocubes: Characterization, photocatalytic activities, and degradation pathway

Shiuh-Tsuen Huang [a], Wenlian William Lee [b,c], Jia-Lin Chang [a], Wu-Sheng Huang [a], Shang-Yi Chou [a], Chiing-Chang Chen [a,*]

[a] Department of Science Application and Dissemination, National Taichung University of Education, Taichung 40306, Taiwan
[b] Department of Occupational Safety and Health, Chung-Shan Medical University, Taichung 40201, Taiwan
[c] Department of Occupational Medicine, Chung-Shan Medical University Hospital, Taichung 40201, Taiwan

ARTICLE INFO

ABSTRACT

The strontium titanate, SrTiO₃, nanocubes are synthesized by the autoclave hydrothermal method under the alkaline condition with TiO₂ and Sr(OH)₂·8H₂O as the starting materials at various reaction temperatures, various NaOH concentration and reaction duration time. The FE-SEM results indicate that the reaction temperature has strong influence on the granular size of SrTiO₃ (STO). The EDS results for STO giving the Sr/Ti atomic ratio of *ca.* 1 for all prepared compounds confirmed the formation of STO and were comparable to the HR-XPS results. The photo-degradation efficiency of the crystal violet (CV) dye by STO is performed under the UV light irradiation, various pH reaction media conditions and the dark room condition for comparisons. STO shows the optimal photo-degradation efficiency when the catalyst is prepared at 130 °C. The degradation intermediates are separated and identified by the HPLC-ESI-PDA-MS in order to propose the possible photo-degradation pathways based on the concentration ratio variations of intermediates during the reaction course of time. The *N*-demethylation reaction occurs to give a consecutive series of intermediates with triphenylmethane (TMP) chromophore (588.3–541.0 nm), accompanied by the oxidative reaction occurring at the central carbon of CV which gives another series of intermediates with diaryl-ketone chromophore (377.2–339.1 nm) and 4-aminophenol (308.9–278.1 nm). The peaks of concentration ratio for the consecutive formation intermediates along the time course further confirm the proposed pathways.

© 2014 Taiwan Institute of Chemical Engineers. Published by Elsevier B.V. All rights reserved.

1. Introduction

From an ecological and physiological point of view, the elimination of toxic chemicals from wastewater is currently one of the most crucial subjects in pollution control. The textile industry presents a global pollution problem owing to the dumping or accidental discharge of dye wastewater into water ways, resulting in a major impact on the quality and esthetics of water resources. The World Bank estimates that 17–20% industrial water pollution comes from textile dyeing and treatment [1]. This percentage represents an appalling environmental challenge for clothing designers and other textile manufacturers. The large amount of dye used at the dyeing stage in textile manufacturing processes represents an increasing environmental danger due to their refractory carcinogenic nature. Particularly, triphenylmethane (TMP) dye is consumed heavily in paper, leather, cosmetic and food industries for the coloring of oil, fats, waxes, varnish, and plastics [2,3]. The photo-cytotoxicity of TMP dye, based on the production of the reactive oxygen species, is intensively studied with the regard of the photodynamic treatment [4]. However, there is a great concern about the thyroid peroxidase-catalyzed oxidation of the TMP dye because the reactions might form various *N*-de-alkylated aromatic amines, whose structures are similar to aromatic amine carcinogens [5]. Hence, a new method of treatment should be developed to overcome the toxic-problems caused by dye wastewater. Recently, the application of semiconductors in the advanced oxidation process (AOP) has gained wide interests for the treatment of dye wastewater owing to its good degradation efficiency, low toxicity and physical and chemical properties. AOP refers to a set of chemical treatment procedures designed to remove organic and inorganic materials from wastewater by oxidation.

Semiconductor photocatalytic has received much attention for counteracting the environmental degradation and being a potential

* Corresponding author. Tel.: +886 422183406; fax: +886 422183560.
  E-mail addresses: ccchen@mail.ntcu.edu.tw, ccchen@ms3.ntcu.edu.tw
(C.-C. Chen).

solution to the worldwide energy shortage. Global crises of environment and energy have been the issues for decades. Among the various solutions, semiconductor particles used as the photocatalysts for decomposing water polluted by organic [6] and for hydrogen evolution [7] have been explored by scientists since titanates were first described as a catalyst for photochemical water splitting [8]. In recent years, environmental issues have become increasingly more important. Numerous treatment technologies have been developed for the environmental remediation, for example, adsorption methods, ion-exchange methods, membrane separation, and photocatalysis [9,10]. Among these types of methods, photocatalysis, in particular, has been intensively studied due to its simplicity, low cost, and high removal efficiency. TiO_2 is broadly used as a photocatalyst for degrading a wide range of organic pollutants because of its nontoxicity, photochemical stability, and low cost [6,7,11]. As compared to TiO_2, titanates exhibit an inherently chemical reactivity, which is beneficial for designing complex titanate-based composites. So far, titanate-based photocatalysts have been achieved, such as $CaTiO_3$ [12], $SrTiO_3$ [13–17], $BaTiO_3$ [18,19], $BaTi_2O_5$ [20], In_2TiO_5 [21], $MnTiO_3$ [22], and $CdTiO_3$ [23]. Some of them display good photocatalytic activity and chemical stability. The fabrication of perovskites (ABO_3) is of great scientific and technological interests for their ferroelectric, pyroelectric, piezoelectric, dielectric, and catalytic properties. Herein, aiming at the synthesis of alkaline earth titanates $MTiO_3$ (M = Sr, and Ba) with adjustable morphology, the high activity of titanate nanopowder is utilized.

STO has been used for water splitting and the decomposition of organic pollutants under UV irradiation. More interestingly, STO offers favorable energy for photocatalysis since its conduction band edge is 200 mV more negative than TiO_2. For STO, the thermodynamically stable form at room temperature is cubic. STO has been synthesized through a variety of methods, including hydrothermal synthesis [15,24], conventional solid-state reaction [25], inverse micelle micro-emulsion method [26], sol–gel method [12], molten salt synthesis [27], and nonaqueous route [28]. Recently, perovskite-type structure compounds have emerged from a hydrothermal reaction as an important conformation. Single-crystalline STO nanorods have been accomplished by asolution-based decomposition of bimetallic alkoxide precursors [29]. STO nanotubes have been generated from a hydrothermal reaction by using titanium oxide nanotubes as a precursor [30]. Porous STO nanostructure has been achieved by an amount of NaOH and titanate nanotubes under $SrCl_2$ saturated solution being placed in a Teflon-lined vessel [31]. Therefore, it would be highly desirable for developing a general approach to fabricate STO with controllable morphology and size. Recently, Wei et al. [32] developed density functional characterization of the electronic structure and optical properties of N-doped, La-doped, and N/La-codoped $SrTiO_3$. The results indicated that the optimal doping model was N/La-codoping with La at Sr site for both energetic and high photocatalytic activity under visible light, in which existed a DAP recombination and thus the charge balance was kept. For this optimal codoped $SrTiO_3$ system, oxygen vacancies associated with N-doping were not required and the overall energy cost for doping decreased, compared with that of N-monodoping.

Generally speaking, the activity of heterogeneous catalysts is basically influenced by crystal phase, size, surface area, and crystallinity [33,34]. Nano-particulate photocatalysts have the advantages of large surface area and short diffusion distance of photo-excited electrons to the surface. Their morphology and outer surface also affect their photocatalytic activity [35]. In this regard, the precise control of the size and shape of $SrTiO_3$ is critically important for evaluating the shape-dependent photoreactivity and developing high-performance photocatalyst. However, in spite of the previous extensive efforts, such a precise

control of their size and shape has been fragmented and limited. However, morphology control has not been adequately achieved yet. In the present study, the precise control of morphology of $SrTiO_3$ nanoparticles has been established in basic aqueous solution. The evaluation of photocatalytic activity of nano-cubic particles will be accomplished.

CV is a TMP dye, which has been extensively used as a biological stain, antimicrobial agents, a commercial textile dye, dermatological agent, targetable sensitizers [36], and veterinary medicine. However, the wastewater containing CV not only causes coloration of water, but also harms the aquatic life and human health. Therefore, there are both health and environmental concerns on this particular dye. This causes a need for the development of efficient, energy-saving and inexpensive dye wastewater treatment processes. In this study, $P25\text{-}TiO_2$, $Sr(OH)_2$, and NaOH are used as the precursors, and the nano-cubes of STO are successfully prepared by autoclave hydrothermal methods at different reaction temperature and time. Besides, the identification of the reaction intermediates is focused and some light is shaded on the mechanistic details of photodegradation of CV dye in the STO/UV process, which in turn can serve as the foundation for future application.

2. Experimental

2.1. Reagents and materials

$P25\text{-}TiO_2$ (Degussa Co. Ltd.; *ca.* 80% anatase, 20% rutile; particle size, *ca.* 20–30 nm; BET area, *ca.* 55 $m^2\,g^{-1}$), $Sr(OH)_2\cdot8H_2O$ (Acro Co. Ltd.; assay $\geq$98%), chloride salt of crystal violet (TCI; assay $\geq$99%), NaOH and CH_3COONH_4 (Osaka Co. Ltd.; guaranteed reagent), HNO_3 (JIS Co. Ltd.; extra pure), Acetone (Merck Co. Ltd.; HPLC-grade), and CH_3OH (J. T. Baker Co. Ltd.; HPLC-grade) were used as the starting materials. De-ionized water used for this study was purified with a Milli-Q water ion-exchange system (Millipore Co.) for a resistivity of $1.8 \times 10^7\,\Omega$ cm. The $P25\text{-}TiO_2$ nanoparticles were supplied by Degussa.

2.2. Preparation of photocatalysts

The nano-cubic STO was synthesized in a beaker by adding 0.1 g $P25\text{-}TiO_2$ and 10 mL NaOH aqueous solution (1, 3, 5, and 10 M) respectively to 0.35 g $Sr(OH)_2\cdot8H_2O$. The mixture was transferred to a Teflon-lined autoclave (capacity: 23 mL) and heated to 100 °C (or 130, 150, and 180 °C) in 24 h (or 48, 72, and 96 h). The material was washed with distilled water, filtered and finally dried in air at 60 °C. There were different reaction conditions (including the concentration of NaOH, reaction time, and temperature), as shown in Table 1, being prepared, namely SR-1-24-130 to SR-3-72-150 for STO samples, respectively.

2.3. Instruments

Waters ZQ LC/MS system, equipped with a binary pump, a photodiode array detector, an autosampler, and a micromass detector, was used for the separation and identification. The HPLC-PDA-ESI-MS system consisted of a Waters 1525 binary pump, a 2998 photodiode array detector, and a 717 plus autosampler. Besides, a ZQ2000 micromass detector and an Atlantis TM dC18 column (250 mm × 4.6 mm i.d., dp = 5 μm) were used for the separation and identification. The column effluent was introduced into the ESI source of the mass spectrometer.

X-ray powder diffraction (XRD) patterns were recorded on a MAC Science, MXP18 X-ray diffractometer with Cu Kα radiation in a 2θ range 20–80° at a scanning speed of 4° min^{-1}, operated at 40 kV and 80 mA. Field emission scanning electron microscopy

Table 1
Summary of samples prepared from hydrothermal treatment with different concentration of NaOH, synthesis time and temperature.

Catalyst code	Ti precursor	Ba precursor	NaOH concentration (M)	Synthesis time (h)	Synthesis temp (°C)
SR-1-24-130	TiO$_2$	Sr(OH)$_2$	1	24	130
SR-3-24-130	TiO$_2$	Sr(OH)$_2$	3	24	130
SR-5-24-130	TiO$_2$	Sr(OH)$_2$	5	24	130
SR-3-48-130	TiO$_2$	Sr(OH)$_2$	3	48	130
SR-3-72-130	TiO$_2$	Sr(OH)$_2$	3	72	130
SR-3-96-130	TiO$_2$	Sr(OH)$_2$	3	96	130
SR-3-72-100	TiO$_2$	Sr(OH)$_2$	3	72	100
SR-3-72-150	TiO$_2$	Sr(OH)$_2$	3	72	150

(FE-SEM) measurement was carried out with a field-emission microscope (JEOL JSM-7401F) at an acceleration voltage of 15 kV. The prepared catalysts were checked with both energy dispersive spectroscopy (EDS) and high resolution X-ray photoelectron spectrometer (HR-XPS). An HRXPS measurement was carried out with ULVAC-PHI XPS. The Al Kα radiation was generated with a voltage of 15 kV. Attenuated total reflection/Fourier transform infrared (ATR/FT-IR) spectra were collected on a Nicolet 380 FT-IR spectrometer. The investigated spectra range was from 4000 to 450 cm^{-1}. The signal was obtained by averaging 32 scans at the resolution of 4 cm^{-1}. UV–vis diffuse reflectance spectra were recorded on a Scinco SA-13.1 spectrophotometer at room temperature. The BET specific surface areas of the samples were measured with an automatic system (Micromeritics Gemini 2370 C) with nitrogen gas as the adsorbate at the liquid nitrogen temperature.

2.4. Analytical methods for identification of intermediates

The amount of residual dye at each reaction cycle was determined by HPLC-PDA-ESI-MS. The analysis of organic intermediates was accomplished by HPLC-PDA-ESI-MS after the readjustment of chromatographic conditions in order to make the mobile phase (solvent A and B) compatible with the working conditions of the mass spectrometer. Solvent A was 25 mM aqueous ammonium acetate buffer (pH 6.9), and solvent B was methanol. LC was carried out on an Atlantis TM dC18 column (250 mm × 4.6 mm i.d., dp = 5 μm). The mobile phase flow rate was 1.0 mL/min. A linear gradient was run as follows: $t = 0$, $A = 95$, $B = 5$; $t = 20$, $A = 50$, $B = 50$; $t = 35$–40, $A = 10$, $B = 90$; $t = 45$, $A = 95$, $B = 5$. The column effluent was introduced into the ESI source of the mass spectrometer. The quadruple mass spectrometer equipped with an ESI interface with heated nebulizer probe at 350 °C was used with an ion source temperature 80 °C. ESI was carried out with the vaporizer at 350 °C and nitrogen as sheath (80 psi) and auxiliary (20 psi) gas to assist in the preliminary nebulization and to initiate the ionization process. A discharge current of 5 μA was applied. Tube lens and capillary voltages were optimized for maximum response during the perfusion of the CV standard.

2.5. Procedure of photocatalysis

An aqueous STO dispersion was prepared by adding 50 mg STO powder to a 100 mL solution containing the CV dye at appropriate concentration. For the reactions in different pH media, the initial pH of the suspensions was adjusted by adding either NaOH or HNO$_3$ solution. Prior to the irradiation, the dispersions were magnetically stirred in the dark for ca. 30 min to establish the adsorption/desorption equilibrium between the dye, and the surface of the catalyst under ambient air-equilibrated conditions. Irradiations were carried out using C-75 Chromato-Vue Cabinet of UVP, which provided a wide area of illumination from 15-W 365 nm and UV tubes positioned on two sides of the cabinet interior. At the given irradiation time intervals, 5 mL aliquots were collected, centrifuged, and then filtered through a Millipore filter to remove the catalyst particulates. The filtrates were analyzed by HPLC-ESI-MS.

3. Results and discussion

3.1. Effect of NaOH concentration

STO powder, prepared with NaOH concentration in the range of 1–5 M, was characterized by XRD, SEM-EDS, DR-UV and XPS techniques (Table 2) to study the cubic phase and surface modifications of STO. The ratio of Sr/Ti was chosen to be greater than 1 to avoid the presence of secondary phase. Furthermore, Sr/Ti > 1 increased the pH of the solution, which was an important thermodynamic variable for the synthesis of perovskite materials and helped avoid the addition of an alkaline mineralizer to facilitate the formation of STO. According to the thermodynamic calculations of stability diagrams for the hydrothermal Sr-Ti system, high pH and Sr/Ti > 1 were necessary for the synthesis of high purity STO crystals [37].

Fig. 1 shows the XRD patterns of hydrothermally synthesized STO powder with NaOH concentration of 1, 3, and 5 M. It was evident that all of the patterns showed good crystallinity with the diffraction peaks fitting well to the peak positions of a standard cubic perovskite structure [space group: Pm3m] of STO (JCPDS No. 35-734) and those of SrCO$_3$. In the literature [16,17], there were
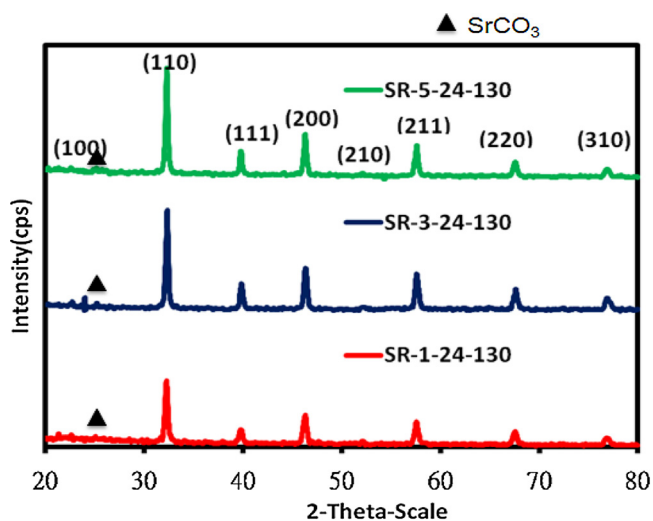
Table 2
Physical and chemical properties of prepared SrTiO$_3$.

Catalyst code	EDS element atomic ratio (%)			XPS element atomic ratio (%)			E_g (eV)	Specific surface area (m^2/g)	Pore size (Å)	Pore volume (cm^3/g)
	Sr	Ti	O	Sr	Ti	O				
SR-1-24-130	13.20	14.20	72.60	–	–	–	3.11	22.96 ± 0.12	11.23 ± 0.09	0.05 ± 0.01
SR-3-24-130	11.92	11.42	76.66	–	–	–	3.13	18.90 ± 0.09	11.65 ± 0.10	0.06 ± 0.01
SR-5-24-130	9.25	9.11	81.64	–	–	–	3.11	18.19 ± 0.11	11.50 ± 0.02	0.06 ± 0.02
SR-3-48-130	14.07	13.97	71.97	15.73	15.72	59.08	3.13	19.09 ± 0.15	11.36 ± 0.03	0.05 ± 0.01
SR-3-72-130	10.46	9.39	80.14	16.87	15.32	56.72	3.10	22.32 ± 0.12	11.77 ± 0.08	0.07 ± 0.01
SR-3-96-130	11.84	11.84	76.32	17.19	16.19	54.03	3.12	19.70 ± 0.09	12.00 ± 0.11	0.06 ± 0.02
SR-3-72-100	14.17	13.31	72.51	–	–	–	3.14	23.18 ± 0.16	11.69 ± 0.13	0.06 ± 0.01
SR-3-72-150	12.15	11.64	76.22	–	–	–	3.11	20.56 ± 0.21	12.02 ± 0.07	0.06 ± 0.01

Fig. 1. XRD patterns of SrTiO$_3$ prepared from hydrothermal NaOH treatment at 130 °C, 24 h with different NaOH concentration.

several papers about the hydrothermal synthesis of the STO compound without the presence of SrCO$_3$ phase. On the other hand, several papers on the presence of secondary phase were also observed [38,39]. A small amount of SrCO$_3$ contamination was noted in almost all the samples due to the introduction of airborne CO$_2$, which would dissolve as CO$_3^{2-}$ and react with Sr^{2+} to form SrCO$_3$ during the pre-treatment and/or the post treatment [40]. The formation of SrCO$_3$, observed in this work, was quite common in the hydrothermal processing as SrCO$_3$ could precipitate at lower pH values than those needed for precipitating STO [41]. According to the thermodynamic stability diagram of Sr-Ti systems, SrCO$_3$ precipitated at lower pH values

than those needed for precipitating STO [37,42]. The XRD results of the as-synthesized STO illustrated the presence of weak peak at 2θ = 24, 35, and 42°, which corresponded to the phase of SrCO$_3$ (JCPDS Card No. 005-0418) and hence confirmed the cubic structure [43]. The STO peaks were very sharp, indicating that the crystalline structure was well developed. The effect of NaOH concentration on the crystal structure and characterization of STO was summarized in Table 2. Fig. 2 shows the SEM images of STO samples prepared, respectively, at various NaOH concentration of 1, 3 and 5 M. The particles agglomerated in a spherical shape with *ca.* 20–200 nm diameters and a little amount of cube-like shape particles. A possible mechanism for the formation of STO by hydrothermal synthesis was the dissolution-precipitation method [44], in which there was a chemical equilibrium between TiO$_2$ and Ti(OH)$_x^{4-x}$. Fig. 2 shows the increase in the particle size of SrTiO$_3$ with an increase in NaOH concentration, which was in accord with the dissolution-precipitation mechanism. Ti(OH)$_x^{4-x}$, a highly active species, could combine with Sr^{2+} to form a new nucleus, and hence, with an increase in NaOH concentration, the chance for forming a new nucleus by Ti(OH)$_x^{4-x}$ increased and led to an increase in the particle size of STO. It could be concluded that the phase formation of cubic STO occurred at the NaOH concentration when TiO$_2$ was used as the Ti(OH)$_x^{4-x}$ precursor. Moreover, the primary particle size of STO prepared using lower [NaOH] was smaller than that prepared using higher [NaOH], which could be ascribed to the smaller particle size of STO prepared by Ti(OH)$_x^{4-x}$ precursor [42]. The agglomeration of STO nanoparticles at higher NaOH concentration promoted the growth of the cubic phase. With subsequent reactions, initial small nanocubes of SrTiO$_3$ are formed by a dissolution–precipitation process [45,46]. The Ti–O bonds on the TiO$_2$ precursor must be broken *via* hydrolytic attack to form the soluble [Ti(OH)$_6$]$^{2-}$. This process is described in Eq. (1). Then, precipitation of SrTiO$_3$ takes place according to Eq. (2). The total reaction is presented in Eq. (3).
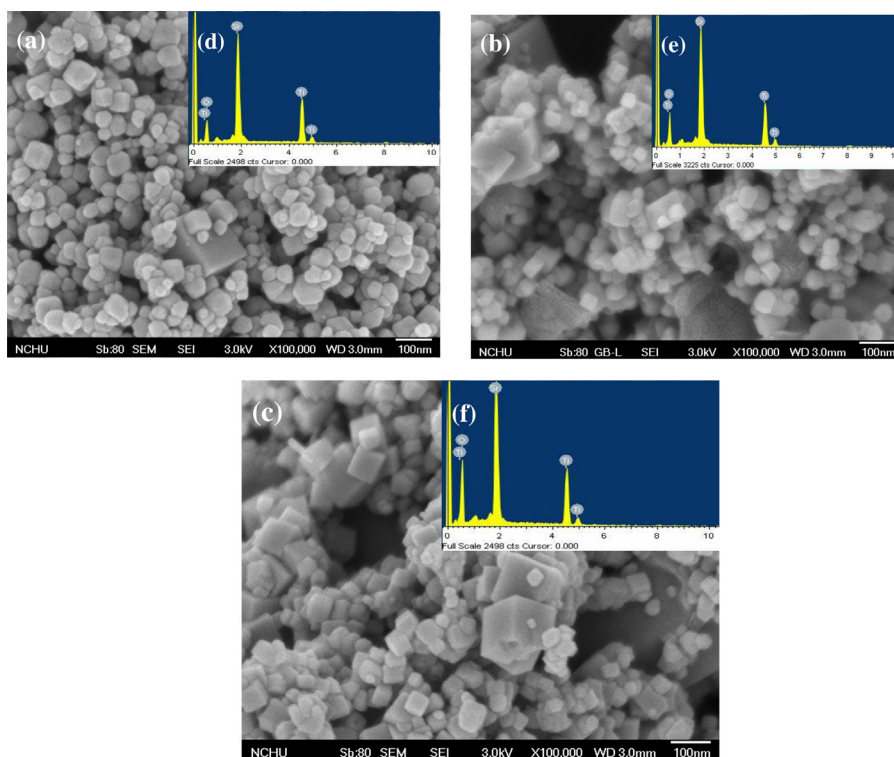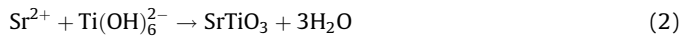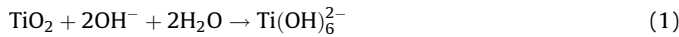

Fig. 2. FE-SEM images and EDS spectra of SrTiO$_3$ prepared from hydrothermal NaOH treatment at 130 °C with different NaOH concentration. (a, d) 1 M; (b, e) 3 M; (c, f) 5 M (24 h).

$$TiO_2 + 2OH^- + 2H_2O \rightarrow Ti(OH)_6^{2-} \qquad (1)$$

$$Sr^{2+} + Ti(OH)_6^{2-} \rightarrow SrTiO_3 + 3H_2O \qquad (2)$$

$$TiO_2 + Sr(OH)_2 \rightarrow SrTiO_3 + H_2O \qquad (3)$$

In Fig. S1 of supplementary data, the adsorption reaction resulted in a decrease about 60–81% in the CV concentration after 36 h, while, in the photocatalytic reaction, the CV was completely decomposed at [NaOH] = 3 M after 36 h. In the following experiment, [NaOH] at 3 M STO was chosen as the optimum photocatalyst.

3.2. Effect of synthesis time

The effect of synthesis time on the formation of crystalline STO was also studied by performing the experiments at different reaction time ranging from 24 to 96 h at 130 °C with [NaOH] = 3 M. The XRD patterns as shown in Fig. S2 confirmed the cubic phase of STO. When STO prepared was treated for 24–96 h, a new peak (SrCO₃) appeared, but disappeared at 96 h. Fig. 3 shows the FT-IR spectrums at different synthesis time. The characteristic absorption at 3435.0 cm^{-1} [47] was assigned to the OH stretching vibration. The infrared spectrum of a carboxylate group, CO_3^{2-}, showed the characteristic doublet absorption due to the asymmetric and symmetric stretching vibrations at 877.45, 1071.26 and 1446.35 cm^{-1} [48], respectively. The IR spectrum was very complex, presenting the bands at 3435 cm^{-1} (O–H stretching modes in crystallization water) [49], 1384.64 and 1636.30 cm^{-1} (carboxylate group stretching modes) [48], 1260 cm^{-1} (C=O stretching modes in COO–Sr), and 850, 582.4 and 450 cm^{-1} (Ti–O vibrational modes) [50]. In Fig. S3, SEM micrographs indicated differences size crystal in the morphology at 24 and 96 h. This phenomenon could be attributed to the Ostwald ripening process of the precursor $SrTiO_3(H_2O)_x$ of the final product $SrTiO_3$, because smaller particles were less stable and the growth of larger particles was energetically favorable. The Ostwald ripening process was determined by both kinetic and thermodynamic effects. During the Ostwald ripening process, larger $SrTiO_3(H_2O)_x$ nanoparticles grew under the conditions of consuming smaller ones in the synthesis process of the precursor $SrTiO_3$. The formation of smaller $SrTiO_3(H_2O)_x$ nanoparticles was kinetically controlled, because their nucleation process was easy. However, after a period of time, larger $SrTiO_3(H_2O)_x$ nanoparticles would grow, due to the thermodynamic conditions [17,51]. This was an energetically favorable process for the growth of larger nanoparticles due to curvature phenomena. The crystal size was larger by extending the processing time; and, the particle size was not significant different from the cubic crystalline. The results are summarized in Table 2. At the early stage of the reaction, hydroxide ions produced more nuclei and formed smaller particles, which grew larger at the prolonged time.

XPS revealed certain mismatch in the stoichiometry and also different chemical composition of the surfaces for different samples. Fig. 4 displays Sr 3d$_{5/2}$, O 1s and Ti 2p photoemission spectra of the coatings as well as the reference feedstock powder. The binding energy of Ti 2p$_{3/2}$ peak (457.400–457.531 eV) was in good agreement with previous XPS studies on STO [52,53]. The O 1s spectra revealed several components. The O 1s spectrum of the feedstock powder could be de-convoluted into a component at the energy range of 528.550–528.735 eV, which corresponded to STO, and a component at 530.956 eV, which was previously identified as belonging to hydroxyl groups typical for the adsorbed water [54]. Taking into account merely the low energy component of O 1s, the intensities of the Sr, Ti, and O core level peaks gave an element ratio Sr:Ti:O equal to 1:1:3, in accordance with the expected stoichiometric value. On the other hand, Sr 3d$_{5/2}$ spectra indicated that strontium was in a different chemical state in all samples. The Sr peaks could be assigned at the binding energies of 132.007–132.141 eV.

The absorbance of the UV–vis diffuse reflectance spectrum for the nanoparticles is shown in Fig. 5. From the pattern, the band gap could be calculated using the equation, $E_g(eV) = 1240/\lambda$ (nm). Band gap (E_g) of nano-STO was estimated to be approximately 3.10 eV and 3.14 eV, respectively, implying that photocatalytic properties might exist under the UV light irradiation. The band gap value reported for particles at 3.35 eV [55] depended on powder and processing details. In addition, the BET specific surface area, pore volume, and pore size showed 18.19–22.32 m²/g, 0.05–0.07 cm³/g, and 11.23–12.02 Å for all samples (Table 2). It was known that the size of nanoparticles had significant effects on the photocatalytic properties due to the variation of surface area, number of active sites and so on [56]. The smaller particle size of nanoparticles would induce to a larger surface area (more active sites) to enhance the photocatalytic activity. The SR-3-72-130 sample had the largest BET. Thus, the larger BET sample might play a role in enhancing the photocatalytic activity.
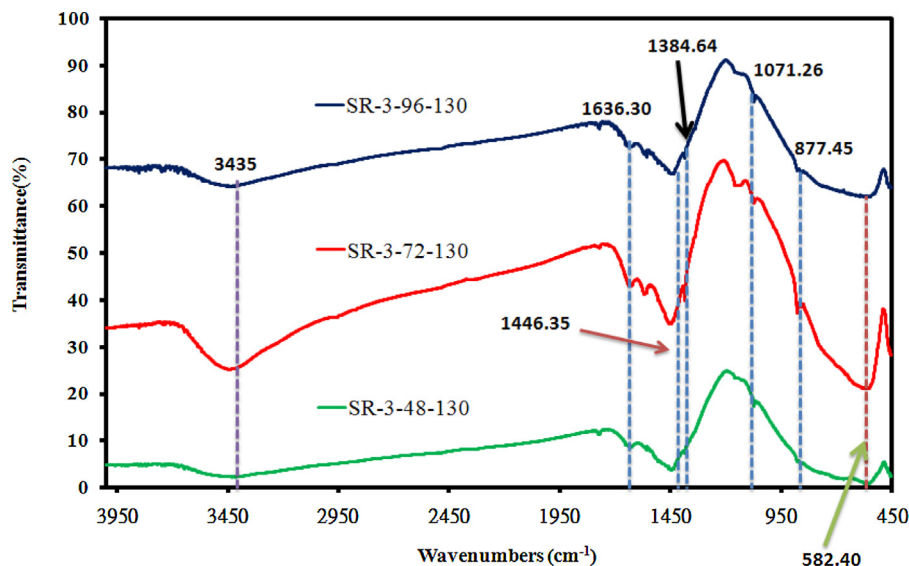

Fig. 3. FT-IR spectra of SrTiO₃ prepared from hydrothermal NaOH treatment at 130 °C with different synthesis time, 48, 72 and 96 h, ([NaOH] = 3 M).
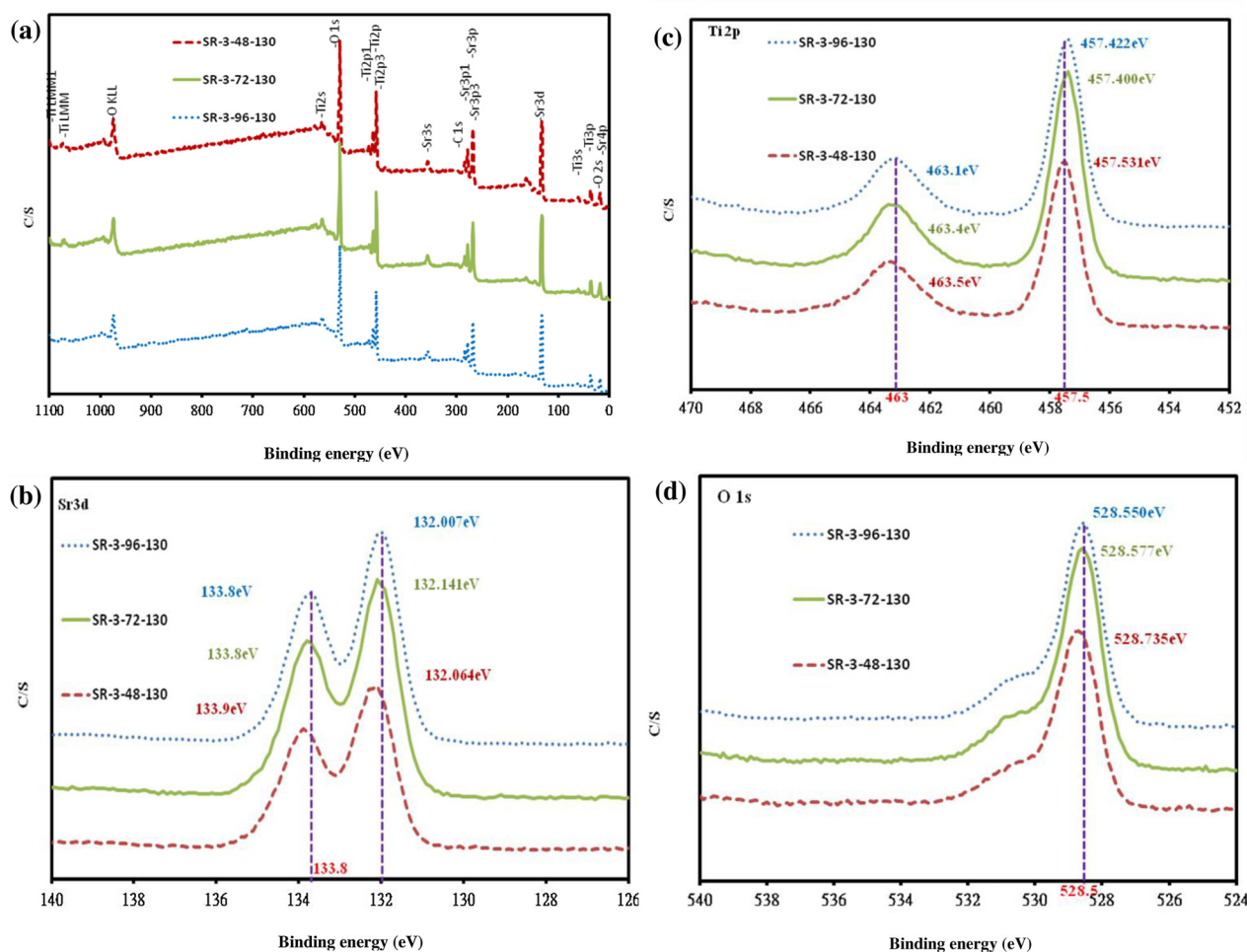
Fig. 4. High resolution XPS spectra of SrTiO$_3$ prepared from hydrothermal NaOH treatment at 130 °C with different synthesis time, 48, 72 and 96 h, ([NaOH] = 3 M). (a) Suls; (b) Sr 3 d; (c) Ti 2p; (d) O 1 s.

Moreover, the band gap energy is also correlated to the photocatalytic activity [57]. The lower band gap has a positive effect on the photocatalytic activity because the lower source energy is needed for arousing a photocatalytic reaction. It means that less energy is needed for activating the nanoparticles to generate excited electron/hole pairs and then induce photocatalytic reactions. In this study, the particle size of nano-STO was a little lower than nano-BTO [19]; however, the result of band gap was on the contrary. It suggested that the higher photocatalytic activity of nano-BTO than nano-STO could be attributed to a lower band gap, which would lead to generate more excited electron-hole pairs to enhance the photocatalytic activity. As for TiO$_2$, it had the lowest band gap and the smallest particle size among them, thus, it had the best photocatalytic efficiency.

Fig. S4 shows the photocatalytic activity of the nanoparticles. The efficiency of photocatalytic degradation on CV was 99% for nano-STO within the first 24 h. The adsorption reaction resulted in a decrease about ∼49% in the CV concentration after 24 h, while, in the photocatalytic reaction, the CV was completely decomposed after 24 h. Compared with TiO$_2$, it suggested that the photocatalytic activity of STO nanoparticles was not bad. With continued development, this kind of nano-materials had the potential to be commercial photocatalysts. In the following experiment, the synthesis time at 72 h of STO was chosen as the optimum photocatalyst.

3.3. Effect of synthesis temperature

STO was prepared at 100, 130, and 150 °C while keeping the rest of the process parameters as [NaOH] = 3 M and the synthesis time as 72 h to study the influence of synthesis temperature on the phase of STO and particle morphology. The XRD patterns of STO were obtained at different hydrothermal temperatures in Fig. S5. The
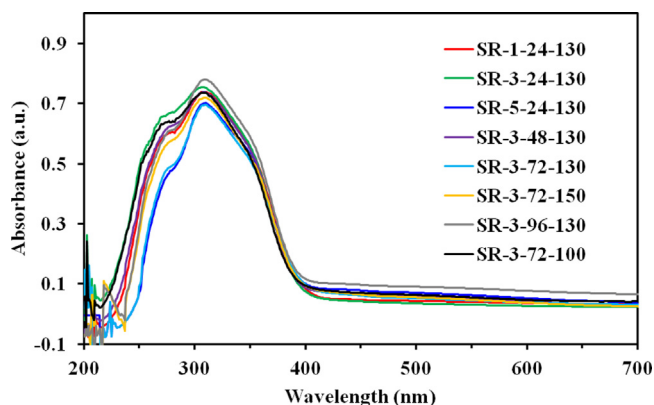

Fig. 5. UV–vis diffuse reflectance spectra of SrTiO$_3$ prepared from hydrothermal treatment with different concentration of NaOH, synthesis time and temperature.

XRD results illustrated the intensity of the peaks increasing with the reaction temperature. There was a possibility of decrease in the unit-cell volume and decrease in density with an increase in the reaction temperature due to the release of lattice hydroxyls [58]. The influence of synthesis temperature is displayed in Table 2. Fig. S6 depicts the SEM of SrTiO₃ prepared at 100, 130, and 150 °C for 72 h. The spherical particles agglomerated into a cubic shape, and the particle sizes estimated from the SEM micrographs were within 20–100 nm in diameter. The increase in the synthesis temperature led to an increase in the particle size, which might explain the stronger agglomeration at higher temperature. However, for STO prepared, the particle size increased with an increase in the reaction temperature, confirming that the particle size of STO was dependent on the synthesis temperature.

In Fig. S7, the adsorption reaction resulted in a decrease about ~36% in the CV concentration after 24 h, while, in the photo-catalytic reaction, the CV was completely decomposed after 24 h. The synthesis temperature at 130 °C of STO was the optimum photocatalyst. To further understand the reaction kinetics of CV degradation, the apparent pseudo-first-order model [59], expressed by $\ln(C_0/C) = k_{app}t$ equation, was applied to the experiments; where k_{app} was the apparent pseudo-first-order rate constant (h^{-1}), C the CV concentration in aqueous solution at time t (mg/L), and C_0 the initial CV concentration (mg/L). Through the first-order linear fit from the data of Figs. S1, S4, and S7 shown in Table 3, the k_{app} of SR-3-72-130 was obtained at the maximal degradation rate of 2.23×10^{-1} h^{-1}, greatly higher than the other composites.

3.4. Effect of photocatalyst concentration

It is important from both the mechanistic and applicational points of view to study the dependence of the photocatalytic reaction rate on the concentration of STO in the CV dye. Hence, the effect of photocatalyst concentration on the photodegradation rate of the CV dye was investigated by employing different concentration of STO varying from 0.25 to 1.0 g L^{-1} in Fig. 6. As expected, the photodegradation rate of the CV was found to increase then decrease with the increase in the catalyst concentration, a general characteristic of heterogeneous photocatalyst, and the results were in agreement with the earlier reports [60]. However, there existed a practical limit of the scattering light (around 1 g L^{-1}), above which the degradation rate would decrease due to the reduction of the photonic flux within the irradiated solution. In the following experiment, the amount of 0.5 g L^{-1} STO was chosen as the optimum photocatalyst.

4. pH effect

The photodegradation rate of the CV dye as a function of reaction pH is shown in Fig. 7. The photodegradation rate of the CV dye was

Table 3
The pseudo-first-order rate constants for the degradation of CV with SrTiO₃ under UV light irradiation.

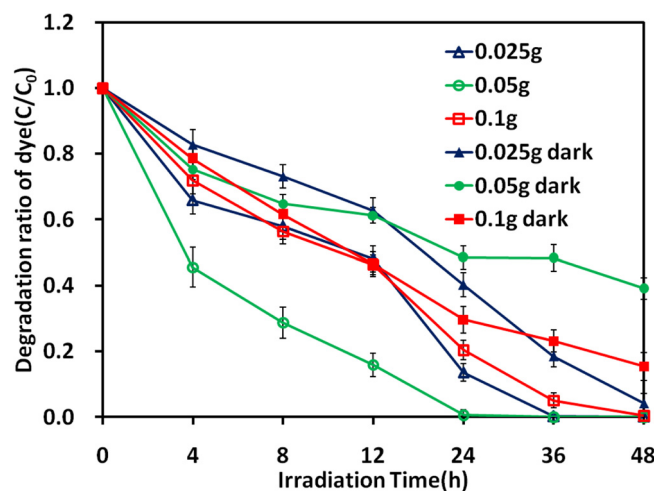| Catalyst code	Rate constant	
	k (h^{-1})	R^2
SR-1-24-130	0.126	0.9601
SR-3-24-130	0.109	0.9204
SR-5-24-130	0.094	0.8585
SR-3-48-130	0.114	0.9758
SR-3-72-130	0.223	0.9738
SR-3-96-130	0.090	0.9666
SR-3-72-100	0.111	0.9609
SR-3-72-150	0.109	0.9567

Fig. 6. Influence of amount of photocatalyst on the CV (10 mg/L) photodegradation rate with SR-3-72-130 photocatalyst (g/100 mL).

found to increase with the increase in the value of pH. Under an acidic condition, it was found that the cationic CV dye was difficult to adsorb onto the STO surface, usually with the active •OH radicals formed in low concentration, and hence the photodegradation process of CV remained very slow. With higher pH values, the formation of active •OH species was favored, as it improved not only the transfer of holes to the adsorbed hydroxyls, but also the electrostatic abstractive effects between the negatively charged STO particles and the operating cationic dyes. Although the CV dye could adsorb onto the STO surface to some extent in alkaline media, the CV dye molecules would change to a leuco compound when the pH value was too high (pH 11). In a good agreement with the adsorption mechanism proposed in reference [61], the results indicated that the STO surface was negatively charged and the CV adsorbed onto the STO surface through the positive ammonium groups.

4.1. Separation and identification of the intermediates

Under the UV irradiation, temporal variations of CV dye photocatalytic degradation process were characterized with HPLC-PDA-ESI-MS. The relevant change in the chromatograms recorded at 580, 350, and 300 nm is illustrated in Figs. S8–S9. Nineteen components were identified with the retention time less than 50 min under the irradiation to 72 h. The CV dye and its relevant intermediates were denoted as species A–J, a–f, and α–γ (Table S1). Except for the initial CV dye (peak A), the intensity of the other peaks increased at first and subsequently decreased, indicating the formation and transformation of the intermediates.

The maximum absorption of each intermediate in the UV/visible spectral region was identified as the peaks A–J, a–f, and α–γ in the Table S1, respectively. The data showed that the absorption spectral bands shifted hypsochromically from 588.3 nm to 541.0 nm (A–J), 377.2 to 339.1 nm (a–f), and 308.9 to 278.1 nm (α–γ). As being seen, the 19 compounds could be distributed into three different aromatic groups, including (i) the intermediates of N-de-methylation of N,N,N′,N′,N″,N″-hexaethylpararosaniline (CV; A), (ii) the intermediates of N-de-methylation of 4-(N,N-dimethylamino)-4′-(N′,N′-dimethylamino) benzophenone (a), and (iii) the intermediates of N-de-methylation of 4-(N,N-dimethylamino) phenol (α), respectively. This hypsochromic shift of the absorption band was possible due to the formation of series of N-de-methylated intermediates in a stepwise manner. For example, λ_{max} of A, B, C, D, E, F, G, H, I, and J were 588.3, 581.0, 574.0, 581.1, 566.6, 570.3, 563.0, 566.4, 555.5 and 541.0 nm; λ_{max} of a, b, c, d, e, and
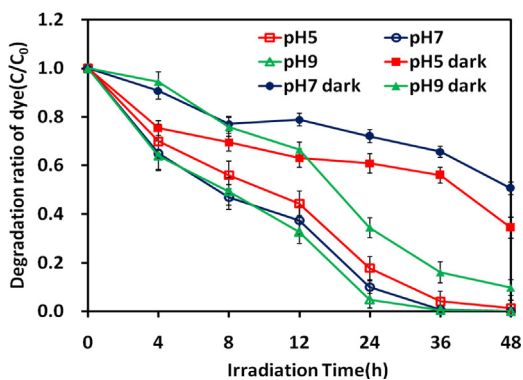
Fig. 7. Influence of pH values on the CV (10 mg/L) photodegradation rate with SR-3-72-130 photocatalyst.

N-de-methylation of CV because of the attack by one of the •OH radicals on the N,N-dimethyl group. The most important situation was that the hypsochromic shift of the absorption band was presumed to result from the formation of a series of N-de-methylated intermediates. As shown above, similar phenomena were demonstrated once using photocatalyst in the photodegradation of Crystal Violet [62] and Acid Blue 1 [63]. Above intermediates were identified as the same with the degradation of CV with STO.

The intermediates of photocatalytic degradation were further identified with HPLC-ESI mass spectrometric method, as shown in Table S1. The molecular ion peaks appeared to be in the acid forms of the intermediates. From the results of mass spectral analysis, the component A, $m/z = 372.40$, was confirmed. The other components were B, $m/z = 358.45$; C, $m/z = 344.35$; D, $m/z = 344.35$; E, $m/z = 330.35$; F, $m/z = 330.22$; G, $m/z = 316.39$; H, $m/z = 316.34$; I, $m/z = 302.29$; J, $m/z = 288.17$; a, $m/z = 269.33$; b, $m/z = 255.28$; c, $m/z = 241.03$; d, $m/z = 241.22$; e, $m/z = 227.27$; f, $m/z = 213.27$; α, $m/z = 138.20$; β, $m/z = 121.05$; γ, $m/z = 110.95$. Moreover, the relative distribution and time reaching maximum concentration of the N-de-methylated and the oxidative cleavage reaction of conjugated chromophore structure intermediates obtained were illustrated. In accordance with the data shown
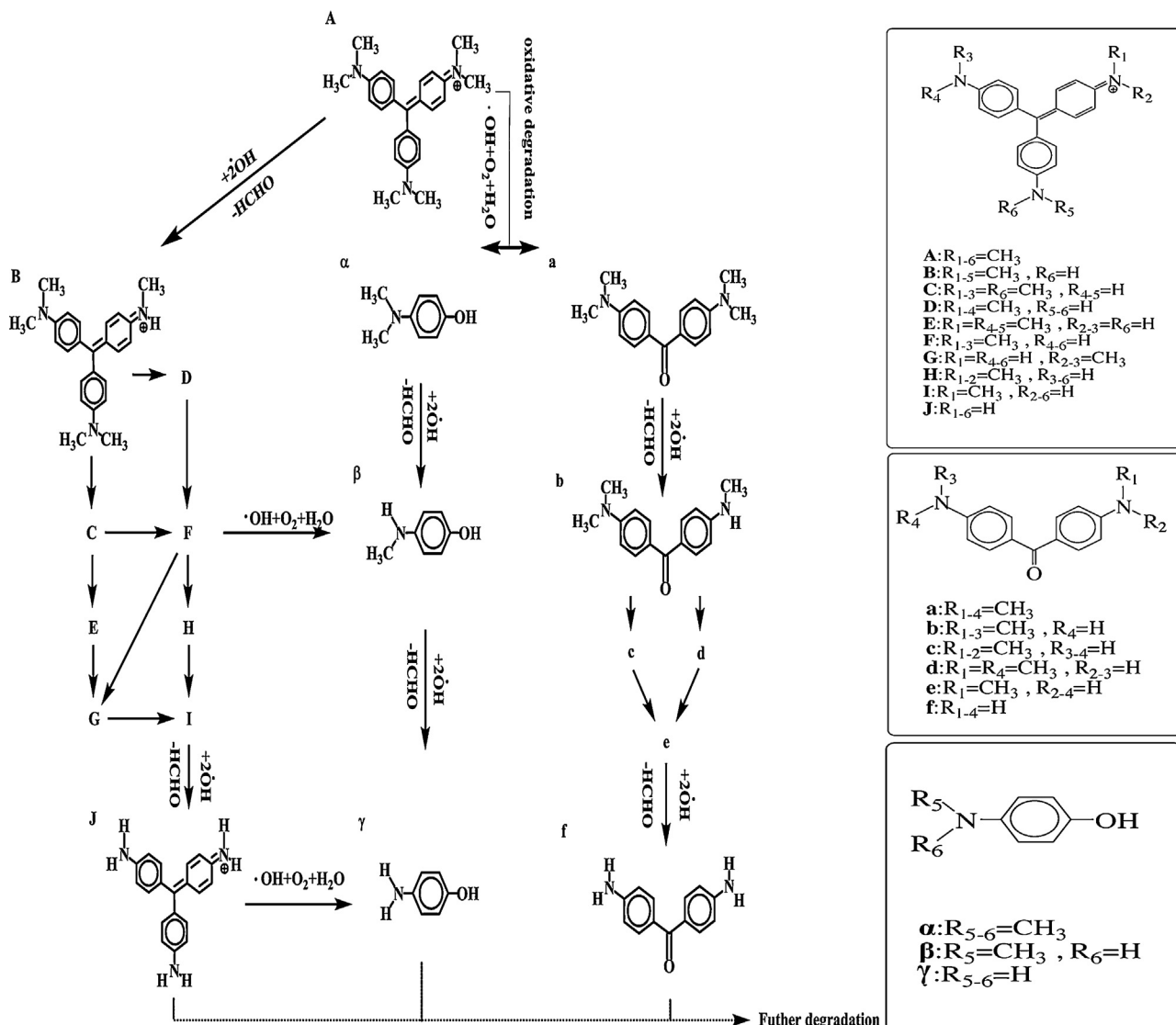
f were 377.2, 366.5, 362.8, 359.8, 357.0, and 339.1 nm; and α, β, and γ were 308.9, 290.0, and 278.1 nm, respectively. Given the identification of N-dimethylated aromatic amines in groups such as A–J, a–f, and α–γ, this was also done for the oxidation of CV dye. The wavelength shift depicted in Table S1 was caused by the
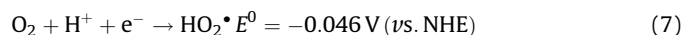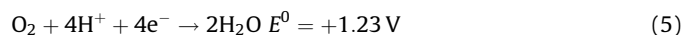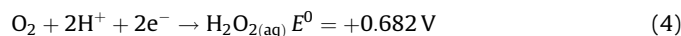

Fig. 8. Proposed photocatalytic degradation mechanism of the CV with SrTiO₃.

in Figs. S8–S9, the successive appearance of the maximum distribution of each intermediate, such as B–J, a–f, and α–γ, indicated the occurrence of the stepwise process of CV N-de-methylation.

4.2. Proposed mechanism of CV degradation

With the UV irradiation, most of the •OH radicals were generated directly from the reaction between the holes and surface-adsorbed H_2O or OH^-. However, the probability for the formation of $O_2^{-\bullet}$ should be much less than that of •OH [64]. Therefore, the N-de-methylation of the CV dye occurred mostly by the attack of the •OH and $O_2^{-\bullet}$ species on the N,N-dimethyl groups of the CV dye. The •OH radicals attacked the mono-, di-, tri-, and tetra-methyl groups resulting in B, C–D, E–F, G–H, and I–J compounds, which could be mainly produced during the N-de-methylation steps. Moreover, both a and α were stepwise N-de-methylated to yield the compound f and γ. It should be emphasized here that upon the mechanisms, all aforementioned processes relied on O_2 to promote the cleavage of the CV conjugated chromophore structure. Although photocatalytic activities strongly depended on the kind of photocatalyst, the mechanistic analysis did demonstrate that the degradation pathway led most oxidative N-de-alkylation processes being preceded by the formation of nitrogen-centered radical, whereas the destruction of the dye chromophore structure proceeded by the generation of the carbon-centered radical [62,63].

It is well known that the potential of multi-electron reduction of O_2 (Eqs. (4)–(5)) is more positive than the single-electron process (Eqs. (6)–(7)) [65]. It seems reasonable to consider such multi-electron reductions being more readily preceded on the surface of catalyst that works catalyze O_2 reduction. The high CV photodegradation activity mediated by STO was due to the promotion of multi-electron reduction of O_2 on the catalyst rather than the single-electron reduction.

$$O_2 + 2H^+ + 2e^- \rightarrow H_2O_{2(aq)} \; E^0 = +0.682 \, V \tag{4}$$

$$O_2 + 4H^+ + 4e^- \rightarrow 2H_2O \; E^0 = +1.23 \, V \tag{5}$$

$$O_2 + e^- \rightarrow O_2^{-\bullet}{}_{(aq)} \; E^0 = -0.284 \, V \tag{6}$$

$$O_2 + H^+ + e^- \rightarrow HO_2^{\bullet} \; E^0 = -0.046 \, V \, (vs. \, NHE) \tag{7}$$

Based on the above experimental results, the degradation pathway was tentatively proposed as depicted in Fig. 8 and detailed pathways in Figs. S10–S11 of appendix. Firstly, the cationic CV dye molecule was adsorbed on the STO surface through charge attraction. Under the UV irradiation, the conduction band electrons flew to the valence band. The hydrolysis or de-protonation reaction of CV dye yielded a nitrogen-centered radical. Once attacked by •OH radicals, N-de-methylation occurred as shown in Fig. S10. The mono-de-methylated dye, B, could also be adsorbed on the STO particle surface and involved in the similar mechanistic process. However, the •OH radicals could attack the conjugated structure and produce a carbon-centered radical. Moreover, the dye derivatives, a and γ, were formed eventually. Moreover, the species a and γ could also be implicated in N-de-methylation to yield b and β (Fig. S11), respectively. The N-de-methylation processes continued to really form N-de-methylated dye, J, f and γ. Further oxidation could lead the ring-opening and the formation of aliphatic oxidation products [66].

5. Conclusion

STO nanocubes are obtained by hydrothermal methods from an aqueous gel suspension. The gel suspension is prepared by a TiO_2 solution with NaOH and adding $Sr(OH)_2 \cdot 8H_2O$. The addition of NaOH leads to spherical particles. The particle size can be tailored in the range 20–100 nm by varying the reaction time, temperature and concentration. A careful control of the synthesis conditions is essential for producing particles with a narrow size distribution. The synthesis conditions at 3 M NaOH, reaction time 72 h, and hydrothermal temperature 130 °C of STO are the optimum photocatalysts. The results indicate those giving the highest photocatalytic activity.

Both N-de-methylation and the destruction of the conjugated structure of the CV dye take place on the STO. This is the first report demonstrating the mechanistic differences of the STO photo-catalyst to wards the photodegradation of TPM dye. Most of the intermediates and final products have been identified by HPLC-ESI-MS and UV–visible spectroscopy.

Acknowledgment

Appendix A. Supplementary data

Supplementary data associated with this article can be found, in the online version, at http://dx.doi.org/10.1016/j.jtice.2014.02.003.

References

[1] Chen SHS, Wu TY, Juan JC. Recent developments of metal oxide semiconductors as photocatalysts in advanced oxidation processes (AOPs) for treatments of dye waste-water. J Chem Technol Biotechnol 2014;2100(86):1130–58.
[2] WileyVCH., Ullmann's Encyclopedia of Industrial Chemistry. Part A27. Triarylmethane and Diarylmethane Dyes. 6th Ed. New York 2001.
[3] Bhasikuttan AC, Sapre AV, Shastri LV. Photoinduced electron transfer in crystal violet (CV+)–bovine serum albumin (BSA) system: evaluation of reaction paths and radical intermediates. J Photochem Photobiol A Chem 2002;150:59–66.
[4] Bonnett R, Martinez G. Photobleaching of sensitisers used in photodynamic therapy. Tetrahedron 2001;57:9513–47.
[5] Cho BP, Yang T, Blankenship LR, Moody JD, Churchwell M, Bebland FA, Culp SJ. Synthesis and characterization of N-demethylated metabolites of malachite green and leucomalachite green. Chem Res Toxicol 2003;16:285–94.
[6] Thompson TL, Yates JT. Surface science studies of the photoactivation of TiO2– new photochemical processes. Chem Rev 2006;106:4428–53.
[7] Tang J, Durrant JR, Klug DR. Mechanism of photocatalytic water splitting in TiO2. Reaction of water with photoholes, importance of charge carrier dynamics, and evidence for four-hole chemistry. J Am Chem Soc 2008;130:13885–91.
[8] Fujishima A, Honda K. Electrochemical photolysis of water at a semiconductor electrode. Nature 1972;238:37–8.
[9] Konstantinou IK, Albanis TA. TiO2-assisted photocatalytic degradation of azo dyes in aqueous solution: kinetic and mechanistic investigations: a review. Appl Catal B Environ 2004;49:1–14.
[10] Ilinoiu EC, Pode R, Manea F, Colar LA, Jakab A, Orha C, Ratiu C, Lazau C, Sfarloaga P. Photocatalytic activity of a nitrogen-doped TiO2 modified zeolite in the degradation of reactive yellow 125 azo dye. J Taiwan Inst Chem Eng 2013;44:270–8.
[11] Frank SN, Bard AJ. Heterogeneous photocatalytic oxidation of cyanide ion in aqueous solutions at titanium dioxide powder. J Am Chem Soc 1977;99:303–4.
[12] Demirörs AF, Imhof A. BaTiO3, SrTiO3, CaTiO3, and BaxSr 1−xTiO3 particles a general approach for monodisperse colloidal perovskites. Chem Mater 21 2009;3002–7.
[13] Kouichi N, Masatoshi K, Ichiro F, Satoshi W. A new approach for the preparation of SrTiO3 nanocubes. Ceram Int 2013;39:3231–4.
[14] Peichuan S, John C, Lofaro JR, William RW, Michael GW, Dong S, Alexander O. Photocatalytic activity of hydrogen evolution over Rh doped SrTiO3 prepared by polymerizable complex method. Chem Eng J 2013;223:200–8.
[15] Zheng Z, Huang B, Qin X, Zhang X, Dai Y. Facile synthesis of SrTiO3 hollow microspheres built as assembly of nanocubes and their associated photocatalytic activity. J Col Inter Sci 2011;358:68–72.
[16] Wei X, Xu G, Ren Z, Xu C, Weng W, Shen G, Han G. Single-crystal-like mesoporous SrTiO3 spheres with enhanced photocatalytic performance. J Am Ceram Soc 2010;93:1297–305.

[17] Silva Jr LFD, Andrés J, Ribeiro C, Moreira ML, Longo E, Mastelaro VR. Long-range and short-range structures of cube-likeshape SrTiO₃ powders: microwave-assistedhydrothermal synthesis and photocatalytic activity. Phys Chem Chem Phys 2013;15:12386–93.

[18] Devi LG, Krishnamurthy G. TiO₂- and BaTiO₃-assisted photocatalytic degradation of selected chloroorganic compounds in aqueous medium: correlation of reactivity/ orientation effects of substituent groups of the pollutant molecule on the degradation rate. J Phys Chem A 2011;115:460–9.

[19] Lee WL, Chung WH, Huang WS, Lin WC, Lin WY, Jiang YR, Chen CC. Photocatalytic activity and mechanism of nano-cubic barium titanate prepared by a hydrothermal method. J Taiwan Inst Chem Eng 2013;44:660–9.

[20] Zhao D, Ying D, Wen C, Pei XM. Synthesis and characterization of single crystalline BaTi₂O₅ nanowires. J Phys Chem C 2010;114:1748–51.

[21] Liu Y, Chen G, Zhou C, Hu Y, Fu D, Liu J, Wang Q. Higher visible photocatalytic activities of nitrogen doped In₂TiO₅ sensitized by carbon nitride. J Hazard Mater 2011;190:75–80.

[22] Song ZQ, Wang SB, Yang W, Li WM, Wang H, Hui Y. Synthesis of manganese titanate MnTiO₃ powders by a sol–gel-hydrothermal method. Mater Sci Eng B 2004;113:121–4.

[23] Handan G, Volkan E, Bircan H, Fahriye, Ahmet G, Ahmet A. Preparation of a new polyaniline/CdOnanocomposite and investigation of its photocatalytic activity comparative study under UV light and natural sunlight irradiation. Ind Eng Chem Res 2013;52:10924–34.

[24] Li Y, Gao XP, Li GR, Pan GL, Yan TY, Zhu HY. Titanate nanofiber reactivity: fabrication of MTiO₃ (M = Ca, Sr and Ba) perovskite oxides. J Phys Chem C 2009;113:4386–94.

[25] Kim SW, Choi HI, Lee MH, Park JS, Kim DJ, Do D, Kim MH, Song TK, Kim WJ. Electrical properties and phase of BaTiO₃–SrTiO₃ solid solution. Ceram Int 2013;39:487–90.

[26] Wang Y, Xu H, Wang X, Zhang X, Jia H, Zhang L, Qiu J. A general approach to porous crystalline TiO₂, SrTiO₃, and BaTiO₃ spheres. J Phys Chem B 2006;110:13835–40.

[27] Mao YB, Banerjee S, Wong SS. Large-scale synthesis of single-crystalline perovskite nanostructures. J Am Chem Soc 2003;125:15718–19.

[28] Niederberger M, Garnweitner G, Pinna N, Antonietti M. Nonaqueous and halide-free route to crystalline BaTiO₃, SrTiO₃, and (Ba, Sr)TiO₃ nanoparticles via a mechanism involving CC bond formation. J Am Chem Soc 2004;126:9120–6.

[29] Miyauchi M. J Phys Chem C 2007;111:12440–45.

[30] Mao YB, Banerjee S, Wong SS. Chem Commun 2003;3:408–9.

[31] Dong WJ, Li X, Yu J, Guo WC, Li BG, Tan L, Li CR, Shi JJ, Wang G. Porous SrTiO₃ spheres with enhanced photocatalytic performance. Mater Lett 2012;67:131–4.

[32] Wei W, Dai Y, Guo M, Yu L, Huang B. Density functional characterization of the electronic structure and optical properties of N-doped, La-doped, and N/La-codoped SrTiO₃. J Phys Chem C 2009;113:15046–50.

[33] Yang HG, Liu G, QiaoSZ, Sun CH, Jin YG, Smith SC, ZouJ, Cheng HM, Lu GQ. Solvothermal synthesis and photoreactivity of anatase TiO2 nanosheets with dominant {0 0 1} facets. J Am Chem Soc 2009;131:4078–83.

[34] Enterkin JA, Poeppelmeier KR, Marks LD. Oriented catalytic platinum nanoparticles on high surface area strontium titanate nanocuboids. Nano Lett 2011;11:993–7.

[35] Kimijima T, Kanie K, Nakaya M, MuramatsuI A. Solvothermal synthesis of SrTiO₃ nanoparticles precisely controlled in surface crystal planes and their photocatalytic activity. Appl Catal B Environ 2014;144:462–7.

[36] Fan HJ, Huang ST, Chung WH, Jan JL, Lin WY, Chen CC. Degradation pathways of crystal violet by Fenton and Fenton-like systems: condition optimization and intermediate separation and identification. J Hazard Mater 2009;171:1032–44.

[37] Lencka MM, Riman RE. Thermodynamics of the hydrothermal synthesis of calcium titanate with reference to other alkaline-earth titanates. Chem Mater 1995;7:18–25.

[38] Moreira ML, Longo VM, Avansi W, Ferrer MM, Andrés J, Mastelaro VR, Varela JA, Longo. Quantum mechanics insight into the microwave nucleation of SrTiO₃ nanospheres. J Phys Chem C 2012;116:24792–808.

[39] Souza AE, Santos GTA, Barra BC, Macedo WD, Teixeira SR, Santos CM, Senos AMOR, Amaral L, Longo E. Photoluminescence of SrTiO₃: influence of particle size and morphology. Cryst Growth Des 2012;12:5671–9.

[40] Guo L, Luo H, Gao J, Guo L, Yang J. Microwave hydrothermal synthesis of barium titanate powders. Mater Lett 2006;60:3011–4.

[41] Lencka MM, Riman RE. Thermodynamic modeling of hydrothermal synthesis of ceramic powders. Chem Mater 1993;5:61–70.

[42] Atkins PW.In: Physical chemistry5th ed. New York: W. H Freeman and Company; 1994.

[43] Fan XX, Wang Y, Chen X, Gao L, Luo WJ, Yuan YP, Li ZS, Yu T, Zhu JH, Zou ZG. Facile method to synthesize mesoporous multimetal oxides (ATiO₃, A = Sr, Ba) with large specific surface areas and crystalline pore walls. Chem Mater 2010;22:1276–8.

[44] Chen KY, Chen YW. Preparation of barium titanate ultrafine particles from rutile titania by a hydrothermal conversion. Powder Technol 2004;141:69–74.

[45] Xin Y, Jiang J, Huo K, Hu T, Chu PK. Bioactive SrTiO₃ nanotube arrays strontium delivery platform on Ti-based osteoporotic bone implants. ACS Nano 2009;3:3228–34.

[46] Kim CW, Suh SP, Choi MJ, Kang YS, Kang YS. Fabrication of SrTiO₃–TiO₂ heterojunction photoanode with enlarged pore diameter for dye-sensitized solar cells. J Mater Chem A 2013;1:11820–27.

[47] Gao YF, Masudav Y, Tetsun Y, Kunihito K. Site-selective deposition and micropatterning of SrTiO₃ thin film on self-assembled monolayers by the liquid phase deposition method. Chem Mater 14 2002;5006–14.

[48] Gopalakrishnamurthy HS, Rao MS, Kutty TRN. J Inorg Nucl Chem 1975;37:891–8.

[49] Adireddy S, Lin CK, Cao BB, Zhou WL, Caruntu G. Solution-based growth of monodisperse cube-like BaTiO₃ colloidal nanocrystals. Chem Mater 2010;22:1946–8.

[50] Cho SG, Johnson PF, Condrate RA. J Mater Sci 1990;25:4738–44.

[51] Hornyak GL, Dutta J, Tibbals HF, Rao AK.In: Introduction to nanoscience. Boca Raton, FL, USA: CRC Press; 2008.

[52] Vander Heide PAW. Surface core level shifts in photo-electron spectra from the Ca, Sr and Ba titanates. Surf Sci 2001;490:616–26.

[53] Ehre D, Cohen H, Lyahovitskaya V, Lubomirsky I. X-ray photoelectron spectroscopy of amorphous and quasiamorphous phases of BaTiO₃ and SrTiO₃. Phys Rev B 2008;771:84–106.

[54] Wei X, Xu G, Ren ZH, Xu CX, Shen G, Han GR. PVA-assisted hydrothermal synthesis of SrTiO₃ nanoparticles with enhanced photocatalytic activity for degradation of RhB. J Am Ceram Soc 2008;91:3795–9.

[55] Chen YH, Chen YD. Kinetic study of Cu(II) adsorption on nanosized BaTiO₃ and SrTiO₃ photocatalysts. J Hazard Mater 2011;185:168–73.

[56] Lin WC, Yang WD, Jheng SY. Photocatalytic degradation of dyes in water using porous nanocrystalline titanium dioxide. J Taiwan Inst Chem Eng 2012;43:269–74.

[57] Manna L, Scher EC, Alivisatos AP. Shape control of colloidal semiconductor nanocrystals. J Cluster Sci 2002;13:521–32.

[58] Qi L, Lee BI, Badheka P, Wang LQ, Gilmour P, Samuels WD, Exarhos GJ. Low-temperature paraelectric-ferroelectric phase transformation in hydrothermal BaTiO₃ particles. Mater Lett 2005;59:2794–8.

[59] Wang WD, Huang FQ, Lin XP. xBiOI-(1−x)BiOCl as efficient visible-light-driven photocatalysts. Scr Mater 2007;56:669–72.

[60] Puangpetch T, Sreethawong T, Yoshikawa S, Chavadej S. Synthesis and photocatalytic activity in methyl orange degradation of mesoporous-assembled SrTiO₃ nanocrystals prepared by sol–gel method with the aid of structure directing surfactant. J Mol Catal A Chem 2008;287:70–9.

[61] Chen CC, Mai FD, Chen KT, Lu CS. Photocatalyzed N-de-methylation and degradation of crystal violet in titania dispersions under UV irradiation. Dyes Pigments 2007;75:434–42.

[62] Lee WW, Chung WH, Huang WS, Lin WC, Lin WY, Jiang YR, Chen CC. Photocatalytic activities of nano-cubic barium titanateby hydrothermal synthesis. J Taiwan Inst Chem Eng 2013;44:660–9.

[63] Chen CC, Fan HJ, Jan JL. Degradation pathways and efficiencies of Acid Blue 1 by photocatalytic reaction with ZnO nanopowder. J Phys Chem C 2008;112:11962–72.

[64] Chen CC, Lu CS. Photocatalytic degradation of Basic Violet 4: degradation efficiency, product distribution, and mechanisms. J Phys Chem C 2007;111:13922–32.

[65] Mrowetz M, Balcerski W, Colussi AJ, Hoffmann MR. Oxidative power of nitrogen-doped TiO₂ photocatalysts under visible illumination. J Phys Chem B 2004;108:17269–73.

[66] Fan HJ, Lu CS, Jan JL, Chiou MR, Chen CC. Comparing differences of degradation pathways between P25-TiO₂ and Pt-TiO₂ mediated photocatalysis under UV irradiation. J Hazard Mater 2011;185:227–35.